



Laser weld geometry and microstructure of cast Uranium-6 wt% niobium alloy

J.W. Elmer^a, A.S. Wu^{b,*}, T. DebRoy^c

^a Materials Engineering Division, Lawrence Livermore National Laboratory, 7000 East Avenue, Livermore, CA, 94550, USA

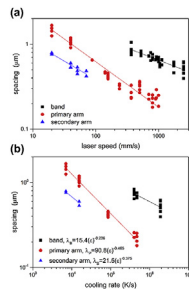
^b Materials Science Division, Lawrence Livermore National Laboratory, 7000 East Avenue, Livermore, CA, 94550, USA

^c Department of Materials Science and Engineering, The Pennsylvania State University, University Park, PA, USA



GRAPHICAL ABSTRACT

A solid-state fiber laser was used to make welds on an as-cast U6Nb alloy with a fixed laser power of 400 W and travel speeds from 20 to 2500 mm/s. Microstructure refinement of approximately 10x was shown to occur as the scan speed increased from 20 mm/s to 2500 mm/s, and the corresponding calculated cooling rate, ϵ , increased from 7.1×10^3 K/s to 2.4×10^6 K/s. Primary and secondary dendrite arm spacing and solidification band spacing measurements in cast U–6Nb plotted on log-log coordinates versus: a) laser scan speed, and b) calculated cooling rate in the center of the six welds that were numerically modeled. Best fit parameters to the cooling rate data are indicated.



ARTICLE INFO

Article history:

Received 24 July 2018

Received in revised form

29 November 2018

Accepted 30 November 2018

Available online 1 December 2018

Keywords:

Welding

Microstructure

Thermodynamic modeling

Microsegregation

ABSTRACT

Laser welding was performed on a U6wt%Nb uranium alloy using a 400 W solid state laser with welding speeds from 20 to 2500 mm/s. This speed range spanned melt pool sizes from traditional welding to surface modification and additive manufacturing. With increasing scan speed, the ratio of weld length relative to depth and width increased, with melt pool lengths being more than 5x greater than the width and 10x greater than the depth at the highest speeds. Keyhole mode welds were shown to occur at low speeds, while conduction mode welds occurred at 700 mm/s or higher as the weld depth dropped off more rapidly than width at higher speeds. Microstructures that form at the boundary between the fusion zone and base metal were observed to have a nonconventional appearance consisting of interpenetrating dark and light contrast phases before cells or dendrites appear. Dendrites with secondary arms form from this boundary in keyhole welds and refine to no visible secondary arms near the weld center. Primary and secondary dendrite arms, where present, were shown to refine in size inversely with cooling rate raised to the 0.465 and 0.375 powers respectively. Dendrites were largely absent from the conduction mode welds at higher speeds, and were replaced by a banded microstructure that appears to form by an oscillatory solidification front mechanism.

© 2018 Elsevier B.V. All rights reserved.

* Corresponding author.

E-mail address: wu36@llnl.gov (A.S. Wu).

1. Introduction

Uranium and its alloys are used to fabricate components where high density or other special properties of uranium are desired. One common uranium alloy that is welded is U-6wt%Nb (U-14.2 at%Nb), which has desirable mechanical properties with added corrosion resistance over pure uranium [1–3]. The enhanced corrosion resistance of this alloy results in a surface that is less prone to oxidation, which is beneficial to welding. U-6wt%Nb further produces a more refined solidification microstructure than pure uranium that is known to grow large grains during welding [4,5].

Uranium and other nuclear metals are most often welded by the electron beam (EB) process in vacuum, which protects them from atmospheric contaminants that would create porosity in the welds [4–6]. Alternatives to EB welding may be beneficial in some cases, however, to date only a small number of publications address alternate welding methods for uranium. For example, arc welding with inert shielding gas has been performed on thin section uranium alloys for nuclear fuel applications [7]. Laser welding, which often competes with EB welding for deep penetration welds, has also been performed, but only one published article is openly available to the author's knowledge of laser welding of uranium alloys using outdated laser welding equipment [8]. This prior work used a multi-kW CO₂ laser operating at 10.6 μm wavelength at speeds between 20 and 120 mm/s to demonstrate feasibility of laser welding of uranium, producing 10 mm penetration at the 12 kW power level. This is a relatively low penetration to power input ratio, which is likely due to a combination of effects such as relatively poor beam quality of the CO₂ laser, interference of the beam by the laser plume, and unusual material properties of uranium compared to more conventional alloys. Higher beam quality of modern solid-state lasers, enhanced plume suppression, and/or reduced pressure laser welding in partial vacuum may all provide new opportunities for laser welding uranium alloys [9–11].

In this study, a solid-state fiber laser was used to weld U6wt%Nb, referred to as U6Nb, over a broad range of laser speeds, with the goal of understanding the influence of laser welding speed on both the weld pool geometry and the resulting microstructure. Using a beam scanning method, two orders of magnitude variations in weld speeds were able to be produced from 20 mm/s to 2500 mm/s. This range encompasses as large a range of melt pool geometries as possible, from traditional welding at lower speeds, to surface treating and additive manufacturing at higher speeds. The transition from a keyhole to a conduction mode weld pool geometry is an important consideration in welding. This transition is known to occur in laser [12,13] and EB [14] welds in conventional alloys as the speed is increased at constant power for example. Keyhole formation is also important for additive manufacturing where it is typically avoided due to the formation of defects in the build as a result of keyhole collapse [15]. One of the main goals of this study was to determine the power/speed conditions where this transition takes place in laser welded U6Nb.

A second goal of this study was to determine the influence of welding speed, and associated cooling rate, on the weld microstructure since this has an important effect on the fusion zone properties [16]. The relationship between weld speed and microstructure is known to originate from a combination of the motion of the liquid pool, the temperature field near the solidification front, and the grain structure of the adjacent solid [17–19]. These studies show that the welding speed and power level affect weld pool geometry and weld cooling rates, and that the cooling rate is, to a first order, controlled by the overall welding speed [20]. However, within a given weld pool, the cooling rate is further influenced by the weld pool geometry since the liquid/solid interfacial velocity is related to the curvature of the trailing weld pool surface [17–19]. By

investigating the influence of laser scanning speed, and its effect on weld pool shape and cooling rate on U6Nb, guidelines may be established for both welding and AM processing conditions in order to produce a given microstructure in U6Nb components.

2. Experimental procedures

2.1. Laser welding

Laser welding was performed using one of the two continuous wave single mode 400 W fiber lasers provided by a SLM[®] 280HL powder bed machine operating at 1.07 μm wavelength. Although this platform is designed for laser powder bed additive manufacturing, it was possible to use this setup to directly weld on solid rectangular U6Nb plates using a laser scanning technique. The plates measured 6.4 mm thick, 25 mm wide, and 152 mm long (0.25 in x 1 in x 6 in), and were machined from a 25 mm thick by 200 mm diameter slice of a cast billet with the weld surface oriented transverse to the cylindrical axis of the casting. The original U6Nb billet was produced using a vacuum induction melting method, followed by shape casting, as generally described in Ref. [2]. This alloy has a nominal composition containing 6.0 wt% Nb, but has typical casting segregation as will be discussed later. Five plates were prepared for welding using conventional machining followed by surface grinding to 32 surface finish. The plates were stored in plastic bags prior to placing them in the AM machine and welding in argon purged atmosphere.

Details of the laser beam, as measured by the manufacturer, indicate that it has a minimum 4σ spot diameter of 76 μm, a Raleigh length of 3.65 mm, and a beam parameter product of 0.395 mm-mrad. Note that the 400 W beam focused into a 76 μm diameter, d, gives a power density of 8.8×10^6 W/cm², which is sufficient to vaporize metals very quickly, and would be expected to create keyhole welding conditions unless the beam is moved at very high speeds [14]. Welds were made by focusing the beam onto the surface of the plate, and were performed in an Ar shielding gas containing 0.09 wt% O₂ during processing as measured by the SLM chamber Lambda sensor. This same gas also provided laminar flow across the plate from behind the weld for laser plasma suppression.

A total of 63 different welds are reported in this study, each 31.8 mm (1.25 in) long, with 12 welds per plate, spaced 6.35 mm (0.25 in) apart in an array as schematically shown in Fig. 1. The 20 fastest welds were built on the same size plate, but in 5 rows spaced 5.1 mm (0.2 in) apart. The spacing was shown to be acceptable based on non-overlap of the small HAZs produced by the high speed welds. All welds were performed at 400 W with laser speeds ranging from 20 to 2500 mm/s as summarized in Table 1 for the low speed welds (<500 mm/s), and Table 2 for the high speed welds (>500 mm/s).

2.2. Specimen preparation and analysis

All of the welds were started and stopped on the surface of the plate, which allowed the weld pool crater to be photographed to determine the length of the weld pool. Cross sections were then prepared through each weld using standard metallographic procedures and etched using 50% phosphoric acid to reveal weld geometry and microstructural details. The weld penetration and width measurements from the cross section are reported in Tables 1 and 2. Representative photos of the top surface and cross sections at different speeds are shown in Fig. 2 and Fig. 3 respectively, indicating the range in weld pool sizes studied in this investigation.

Weld microstructures were further analyzed using scanning electron microscopy using an FEI Nova 600i Nanolab FIB-FESEM, at

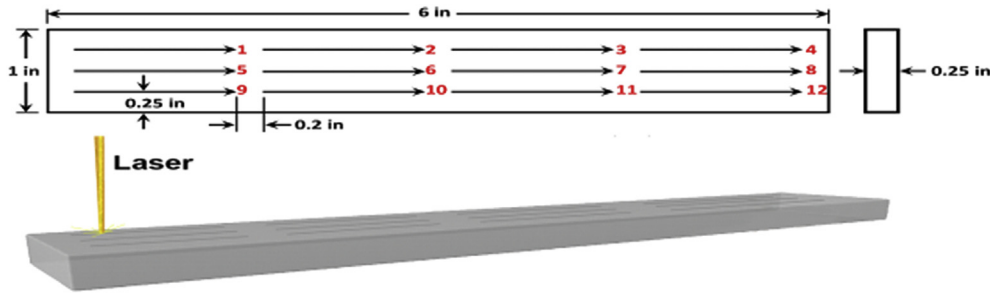


Fig. 1. Schematic layout of the weld locations on the base plate with 3 rows of four welds each.

Table 1

Summary of weld speeds, R, weld energy deposition, D, W, and L, and aspect ratios for the low speed welds. All welds were made at 400 W with a fixed beam diameter of 0.076 mm.

R	E_L	E_o	D	W	L	D/W	L/W	L/D
(mm/s)	(J/mm)	(J/mm ²)	(mm)	(mm)	(mm)			
20	20.00	263.00	1.170	1.350	1.006	0.867	0.745	0.860
21	19.10	251.00	1.270	1.290	1.051	0.984	0.815	0.828
22	18.20	239.00	1.210	1.270	1.032	0.953	0.813	0.853
23	17.30	229.00	1.250	1.260	1.048	0.992	0.832	0.838
24	16.40	219.00	1.180	1.260	1.074	0.937	0.852	0.910
26	15.50	202.00	1.240	1.200	0.985	1.033	0.821	0.794
28	14.60	188.00	1.210	1.190	0.958	1.017	0.805	0.792
29	13.60	181.00	1.100	1.150	0.941	0.957	0.818	0.855
31	12.70	170.00	1.090	1.140	0.854	0.956	0.749	0.783
34	11.80	155.00	1.170	1.100	0.875	1.064	0.795	0.748
37	10.90	142.00	1.090	1.090	0.897	1.000	0.823	0.823
40	10.00	131.00	1.100	1.050	0.911	1.048	0.868	0.828
42	9.46	125.00	1.000	1.010	0.795	0.990	0.787	0.795
45	8.91	117.00	0.987	0.973	0.787	1.014	0.809	0.797
48	8.36	109.00	0.946	0.961	0.856	0.984	0.891	0.905
51	7.82	103.00	0.945	0.936	0.859	1.010	0.918	0.909
55	7.27	95.70	0.952	0.912	0.808	1.044	0.886	0.849
59	6.73	89.20	0.897	0.877	0.762	1.023	0.869	0.849
65	6.18	81.00	0.838	0.884	0.787	0.948	0.890	0.939
71	5.64	74.10	0.811	0.823	0.764	0.985	0.928	0.942
79	5.09	66.60	0.772	0.733	0.781	1.053	1.065	1.012
88	4.55	59.80	0.774	0.750	0.762	1.032	1.016	0.984
100	4.00	52.60	0.662	0.738	0.772	0.897	1.046	1.166
108	3.71	48.70	0.762	0.638	0.821	1.194	1.287	1.077
117	3.42	45.00	0.675	0.611	0.806	1.105	1.319	1.194
128	3.13	41.10	0.647	0.597	0.787	1.084	1.318	1.216
141	2.84	37.30	0.656	0.558	0.747	1.176	1.339	1.139
157	2.55	33.50	0.656	0.514	0.741	1.276	1.442	1.130
177	2.26	29.70	0.543	0.505	0.694	1.075	1.374	1.278
204	1.96	25.80	0.404	0.364	0.719	1.110	1.975	1.780
239	1.67	22.00	0.494	0.427	0.722	1.157	1.691	1.462
289	1.38	18.20	0.485	0.382	0.648	1.270	1.696	1.336
367	1.09	14.30	0.404	0.364	0.608	1.110	1.670	1.505

Table 2

Summary of weld speeds, R, weld energies, D, W, and L, and aspect ratios for the high speed welds. All welds were made at 400 W with a fixed beam diameter of 0.076 mm.

R	E_L	E_o	D	W	L	D/W	L/W	L/D
(mm/s)	(J/mm)	(J/mm ²)	(mm)	(mm)	(mm)			
500	0.80	10.50	0.276	0.331	0.523	0.834	1.580	1.90
550	0.73	9.57	0.248	0.293	0.667	0.846	2.276	2.69
575	0.70	9.15	0.242	0.273	0.631	0.886	2.311	2.61
600	0.67	8.77	0.238	0.262	0.618	0.908	2.359	2.60
625	0.64	8.42	0.224	0.259	0.522	0.865	2.015	2.33
650	0.62	8.10	0.215	0.222	0.649	0.968	2.923	3.02
675	0.59	7.80	0.202	0.218	0.650	0.927	2.982	3.22
700	0.57	7.52	0.158	0.155	0.589	1.02	3.80	3.73
750	0.53	7.02	0.181	0.211	0.495	0.858	2.346	2.74
775	0.52	6.79	0.182	0.200	0.528	0.910	2.640	2.90
800	0.50	6.58	0.186	0.195	0.504	0.954	2.585	2.71
825	0.49	6.38	0.148	0.216	0.392	0.685	1.815	2.65
850	0.47	6.19	0.165	0.211	0.380	0.782	1.801	2.30
875	0.46	6.02	0.162	0.204	0.431	0.794	2.113	2.66
900	0.44	5.85	0.167	0.185	0.597	0.90	3.23	3.57
925	0.43	5.69	0.142	0.186	0.643	0.763	3.457	4.53
950	0.42	5.54	0.082	0.170	0.413	0.482	2.429	5.04
975	0.41	5.40	0.150	0.186	0.518	0.806	2.785	3.45
1000	0.40	5.26	0.164	0.188	0.671	0.872	3.569	4.09
1025	0.39	5.13	0.148	0.179	0.445	0.827	2.486	3.01
1050	0.38	5.01	0.142	0.193	0.596	0.736	3.088	4.19
1075	0.37	4.90	0.138	0.199	0.600	0.693	3.015	4.35
1125	0.36	4.68	0.143	0.182	0.52	0.79	2.86	3.64
1175	0.34	4.48	0.121	0.187	0.391	0.647	2.091	3.23
1250	0.32	4.21	0.127	0.186	0.780	0.683	4.194	6.14
1500	0.27	3.51	0.095	0.186	0.780	0.511	4.194	8.21
1750	0.23	3.01	0.077	0.138	0.788	0.56	5.71	10.23
2000	0.20	2.63	0.066	0.158	0.957	0.423	6.062	14.5
2250	0.18	2.34	0.066	0.158	0.957	0.418	6.057	14.50
2500	0.16	2.11	0.057	0.152	0.821	0.375	5.401	14.40

2.3. Weld modeling

A 3D heat transfer and fluid model was used to simulate the temperature and velocity fields in selected laser welds by solving the equations of conservation of mass, momentum and energy. The details of the governing equations, boundary conditions and the algorithm can be found in previous papers [22–24]. Specific applications of the 3D model for the prediction of weld geometries and temperature distributions in previous laser keyhole weld modeling studies are available with applications to structural steels, stainless steels, Ti–6Al–4V, and refractory metals [12].

This same model was applied to the U6Nb alloy using the laser beam parameters and the thermophysical properties of the alloy as summarized in Table 3, taken from various sources [25–31]. The model was used to solve for seven variables simultaneously: three components of velocity, enthalpy (temperature), pressure, effective thermal conductivity, and effective viscosity of liquid alloy. Computational details used for modeling the laser welds produced

5 kV, and also using an FEI-XL30SFEG, at 5 kV with a 5 mm working distance. Primary and secondary dendrite arm spacing were measured in multiple welds using a line intercept method on images of the polished and etched cross sections. Vicker's microhardness testing was performed using a calibrated microhardness tester. Microsegregation was measured across selected high speed and low speed welds using electron dispersive X-ray spectroscopy (EDAX Genesis EDS), and electron microprobe analysis (EPMA, JEOL-8200, 15 kV). Additional characterization was performed on some welds using a gallium focused ion beam [21] to mill into a U6Nb weld and reveal subsurface microstructural features with electron microscopy. These results were used to analyze Nb microsegregation on length scales with a spatial resolution of approximately 1 μ m diameter beam spot size and an estimated electron penetration depth <400 nm.

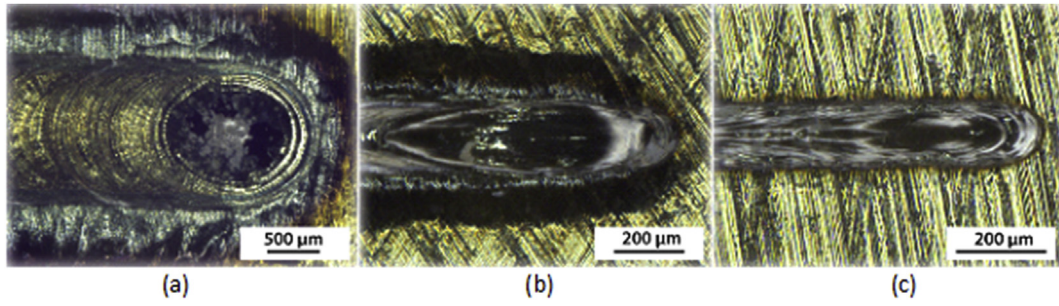


Fig. 2. Photographs of the weld craters from a) weld at 20 mm/s, b) weld at 700 mm/s and c) weld at 2500 mm/s. The welds are moving from left to right in the photos; note the elongation of the weld length relative to the width as the speed increases.

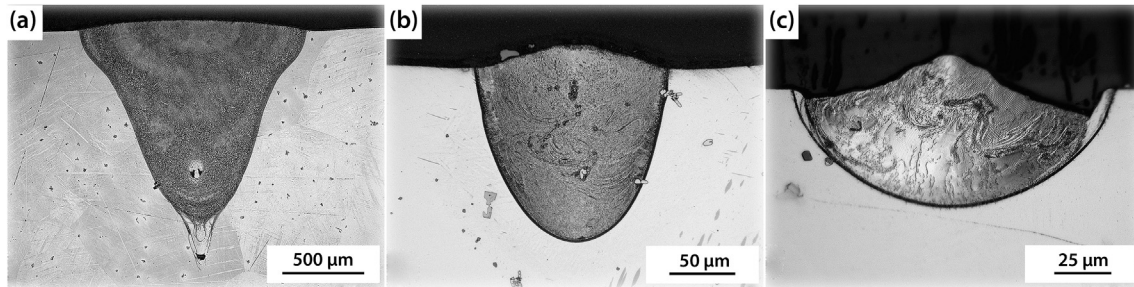


Fig. 3. Comparison of the cross sections of a) the lowest speed weld at 20 mm/s, b) the keyhole transition speed of 700 mm/s, and c) the highest speed of 2500 mm/s. Note the different magnifications used in each micrograph.

in this study are summarized in Table 4, showing that non-uniform grids were used for maximum resolution of variables, with a total of 655,632 grid points (157 × 72 × 58) for calculation. Each laser weld simulation required about 7000 iterations for convergence using a laptop computer.

The resulting model calculated the steady state laser keyhole geometric shape and temperature distribution in the fusion zone (FZ) above the liquidus temperature, the liquid/solid partially melted zone (PMZ) between the liquidus and solidus temperatures, and the heat affected zone (HAZ) below the solidus temperature. The model simulates the steady state weld pool geometric shape, and was verified through experimental weld cross sections at selected weld speeds, as indicated in the comparison between the calculated and experimental cross section for the slowest speed weld at 20 mm/s in Fig. 4.

The location dependent cooling rates within the weld can be

Table 4
Computational details used in the numerical model.

Property and units	Value
Number of grid points in x-direction (length)	157
Number of grid points in y-direction (width)	72
Number of grid points in z-direction (depth)	58
Length of the specimen (cm)	9.1
Width of the specimen (cm)	1.75
Height of the specimen (cm)	0.635

calculated from the product of the local temperature gradient, G , and the local solidification velocity, R_{loc} , as described in more detail elsewhere [17,18]. The temperature gradient at any location of the solid/liquid (S/L) interface of the molten pool can be calculated as follows [17,18]:

Table 3
Welding parameters used for the weld model simulations.

Parameter and units	Value
Laser power (watt)	400
Laser absorption coefficient	0.03
Laser beam diameter (cm)	0.0025
Defocus (cm)	0.35
Laser power distribution	Gaussian
Welding velocity (cm/sec)	2–250
Molecular viscosity of liquid (gm/cm-sec)	0.065
Solidus temperature (K)	1503
Liquidus temperature (K)	1623
Enthalpy of solid at melting point (cal/gm)	61.6
Enthalpy of liquid at melting point (cal/gm)	84.6
Specific heat of solid (cal/gm-K)	$0.032 + 1.81 \times 10^{-5}(T-273 \text{ K})$
Specific heat of liquid (cal/gm-K)	0.039
Thermal conductivity of solid (cal/cm-sec-K)	$0.052 + 6.38 \times 10^{-5}(T-383 \text{ K})$
Thermal conductivity of liquid (cal/cm-sec-K)	0.015
Temperature coefficient of surface tension (N/m-K)	-0.14×10^{-3}

$$G = \|\nabla T\| = \sqrt{\left(\frac{\partial T}{\partial x}\right)^2 + \left(\frac{\partial T}{\partial y}\right)^2 + \left(\frac{\partial T}{\partial z}\right)^2} \quad (1)$$

where T is temperature, x is in the welding direction, y is in the weld width direction, and z is in the vertical weld depth direction, as illustrated in Fig. 5. The local solidification rate, R_{loc} , shown in this figure is the speed normal to the S/L interface on the trailing side of the molten pool. Its value is position dependent and changes from $R_{loc} = 0$ at the maximum weld width to $R_{loc} = R_{max}$ at the centerline on the top surface of the weld, and can be calculated as follows:

$$R_{loc} = R_{max} \cdot \cos \alpha \quad (2)$$

In this equation R_{max} is the scan speed parallel to the scanning direction and represents the maximum solidification rate. The angle α indicates the angle between the scanning direction and the maximum heat flow direction that the grains follow, and is defined by the following relationship:

$$\cos \alpha = \frac{-\partial T / \partial x}{G} \quad (3)$$

The position dependent cooling rate, ε , for selected welds was calculated by the following equation and is used later in this paper to calculate the cooling rates for selected laser welds:

$$\varepsilon = G \cdot R_{loc} \quad (4)$$

3. Results and discussion

3.1. Keyhole to conduction mode transition

Laser and electron beams can produce weld pool shapes that deviate considerably from heat sources such as arcs and flames since the more intense beams can concentrate their heat into much smaller areas [32]. The resulting high power density produces intense localized vaporization of the metal that is being welded, allowing for deep penetration into the base metal through the formation of a vapor cavity into the surface of the metal when power densities exceed approximately 10^5 W/cm² at typical welding speeds [14,32]. The cross-sectional shape of deep, high aspect ratio, welds is narrow at the bottom and wide at the top and has a

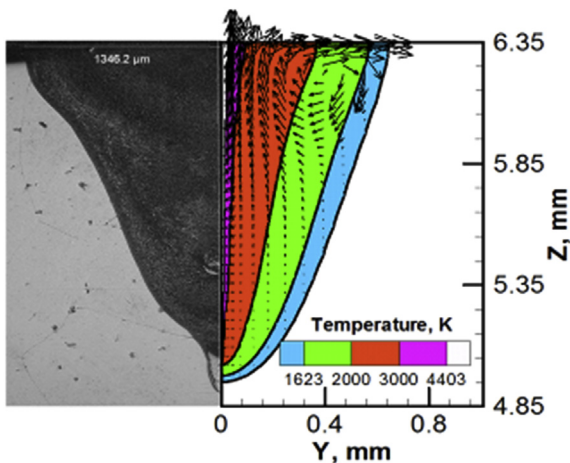


Fig. 4. Comparison between the calculated and experimental cross sections of the slowest speed laser weld at 20 mm/s. Simulated temperatures are indicated by different colors, while fluid flow vectors are indicated by the arrows. (For interpretation of the references to color in this figure legend, the reader is referred to the Web version of this article.)

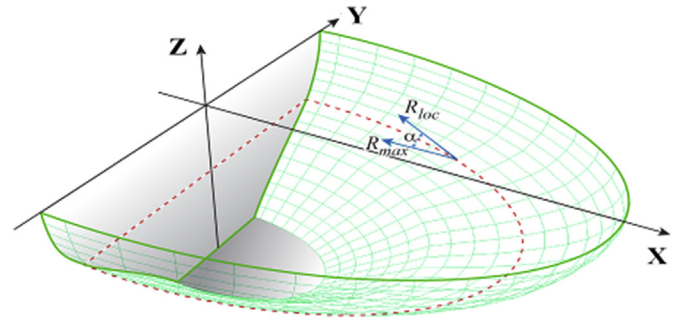


Fig. 5. Illustration of the top back portion of a keyhole weld showing the coordinates used in the model, and the relationship between the local solidification velocity R_{loc} and the maximum scan speed R_{max} .

keyhole-like appearance that gives it its name. Welds are often made in this regime since deep penetrations can be performed with minimal heat input into the part being welded. However, sometimes more shallow penetrations are desired for thin weld joints, surface treating applications [32], and more recently additive manufacturing using lasers and electron beams [33,34]. The shallow welds are often referred to as conduction mode welds since the heat source is distributed on the surface with minimal vapor cavity penetration into the part, allowing for heat conduction to spread the beam's energy in a way that produces a semicircular weld cross section. In order to promote conduction mode behavior, the beam can be defocused to larger diameters to reduce its power density, or it can be moved at higher speeds to spread its energy over longer lengths in the weld direction. Defocusing the beam to larger diameters is often performed in surface treating applications where large areas are to be covered. Moving the focused beam at higher speeds is performed where higher spatial resolution is desired such as in small welds and in additive manufacturing.

In this study the laser beam power and diameter were held constant, while the beam's travel speed was varied from low speeds (welding) to high speeds (surface treating, additive manufacturing) in order to identify the keyhole to conduction mode transition. Weld power, speed and spot size are essential variables in welding that must be carefully controlled in order to produce a consistent weld geometry, and these variables can be combined into useful ratios for comparing welds made under different welding conditions. One ratio compares the beam power, P , to the scan speed, R , and is a measure of how much energy is deposited per unit length of weld, E_L .

$$E_L = P/R \quad (5)$$

Increasing E_L produces deeper and wider welds [14], and in this study E_L was varied from 0.16 J/mm for the highest speed weld at 2500 mm/s, to 20 J/mm for the lowest speed weld at 20 mm/s as summarized in Tables 1 and 2. A second parameter used to characterize the weld is the average energy density, E_o , which is defined as the ratio of E_L to the beam diameter, d .

$$E_o = P/(R \cdot d) \quad (6)$$

E_o represents the average amount of energy deposited per unit area on the surface of the plate being welded and increases with decreasing spot size. E_o can be used as a parameter to estimate the keyhole to conduction mode transition [14]. In this study, E_o was varied from 2.11 J/mm² for the highest speed weld at 2500 mm/s, to 263 J/mm² for the lowest speed weld at 20 mm/s as summarized in Tables 1 and 2. Higher values of E_o correspond to keyhole mode

welding, and the transition from conduction to keyhole mode welds has been shown in other studies to be on the order of 10 J/mm² for electron beam welds in stainless steel and aluminum alloys [14]. The keyhole transition in laser welded U6Nb determined in this study compares favorably to the results from the EB weld study as will be described in more detail later.

Weld depth, D, full width, W, and length of the weld pool, L, were measured using optical microscopy, and the results are summarized in Tables 1 and 2. Note that the weld length is measured from the center of the weld pool to the end of the trailing edge of the weld pool to represent the portion of the weld undergoing solidification. The length measurements were made from photographs of the weld crater on the top surface of the plate as shown in Fig. 2 for high, medium, and low speed welds. In these photographs, the welds are moving from left to right. It is clear that the weld width becomes smaller relative to the weld length as the weld speed increases. This is a common feature of all welds whereby the weld pool shape on the top surface changes from circular to oval to teardrop as the speed increases due to the spreading of the heat along the weld surface as the speed is increased [14,16–18].

Fig. 3 compares several weld cross sections, representing the lowest speed, a medium speed, and the highest speed welds made in this study at different magnifications for clarity. Fig. 3a shows the lowest speed weld at 20 mm/s, which has a relatively small aspect ratio keyhole and spiking at the root of the keyhole. This weld is 1.17 mm deep and 1.35 mm wide with a D/W aspect ratio close to unity. Note the weld depth measurements were made neglecting spiking, as this is an unstable feature that is not consistent along the length of the weld. Fig. 3b shows the medium speed weld at 700 mm/s, which is shallower with a depth of 0.18 mm and narrower with a width of 0.21 mm. Although the aspect ratio of this weld is similar to the low speed weld, the shape is somewhat different, being more semicircular without evidence of spiking. Fig. 3c shows the highest speed weld at 2500 mm/s, which has a semicircular cross section, characteristic of a conduction mode weld. This weld is only 0.057 mm deep and 0.152 mm wide, and is more than two orders of magnitude smaller in cross sectional area than the lowest speed weld, and displays some undercutting at the toe of the weld and humping above the plate surface. Convection swirls are observed in the highest speed weld, and this weld shows significantly different microstructures than the slow speed welds as will be discussed later.

The measured weld depths and widths are plotted in Fig. 6 for the 63 welds reported in this study. This plot is shown on log-log coordinates in an attempt to linearize the weld depth versus travel speed relationship. At low speeds, the depths, D, and full weld widths, W, are similar, giving the welds a keyhole shape with an aspect ratio, D/W, close to unity. The keyhole type welds made here at low speeds have only moderate aspect ratios compared to similar welds made in stainless steel and aluminum at similar energy densities of approximately 200 J/mm² that may have 5x this aspect ratio [14]. The reduced aspect ratio of the U6Nb welds is believed to be at least partly related to the material properties such as high vaporization temperatures of U and Nb, and the high density of the alloy relative to stainless steel and aluminum. A high vaporization temperature requires more of the beam's energy for the formation of a keyhole and the higher density requires more pressure to sustain the keyhole. These effects decrease the depth of the keyhole relative to lower vaporization point and lower density metals and alloys [12]. The U6Nb welds were further shown to maintain this aspect ratio as the speed is increased up to approximately 700 mm/s, even though the welds are becoming shallower at higher speeds. For speeds above 700 mm/s, the weld width trend begins to deviate from the weld depth trend where a distinct

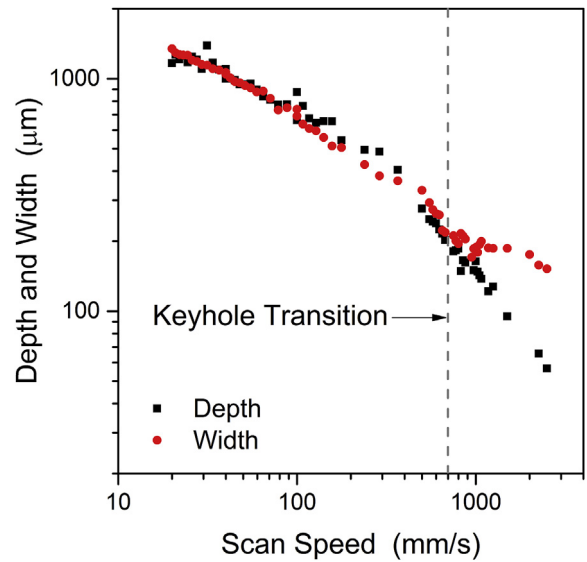


Fig. 6. Weld depths and widths plotted on log-log coordinates to identify the keyhole to conduction mode transition in laser welded U6Nb. The slope of the scan speed curve near the keyhole transition depth is similar to the value of 0.625 (shown on plot) for stainless steel and aluminum alloy keyhole electron beam welds [14].

transition to lower aspect ratio welds occurs. This transition from high to low aspect ratio welds represents what we are defining here as the transition from keyhole to conduction mode welding and is an important transition point for the laser welding conditions used in this study. Note that the average energy density, E₀, for this 400 W beam at 700 mm/s calculates to be 7.5 J/mm², which is very similar to the keyhole to conduction mode transition determined for stainless steel (10 J/mm²) and aluminum alloy (6 J/mm²) electron beam surface scans [14].

There are three weld aspect ratios D/W, L/W, and L/D that can be used to describe the geometric shape of the weld pool. Fig. 7 plots these aspect ratios versus scan speed on log-log coordinates. The D/W aspect ratio, shown by the black squares, has a value of approximately unity for the keyhole welds made in this study. Thus, as the weld depth decreases with increasing scan speed, the width

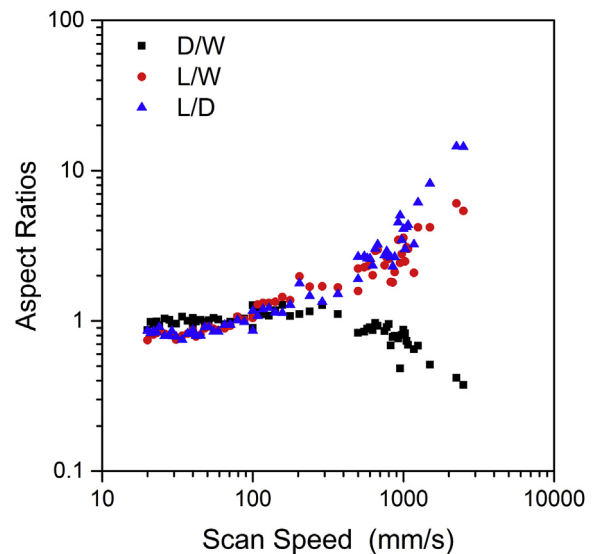


Fig. 7. Aspect ratios D/W, L/W, and L/D, related to Depth, Width and Length of the weld, plotted versus scan speed.

decreases proportionally up to the keyhole transition at about 700 mm/s. After the keyhole transition, the weld depth decreases more rapidly than the width with scan speed, resulting in a decrease in D/W to 0.375 at the highest speed of 2500 mm/s. The L/W and L/D ratios both follow a different trend than D/W . Fig. 7 shows that L/W and L/D both start out with values of approximately 0.75 at low speeds and increase gradually up to values of about 2 near the keyhole transition. Increases in the L/W and L/D ratios are the result of the weld becoming more tear-dropped shaped on the top surface, as the length of the weld increases relative to its width with increasing speed as the heat spreads out more along the direction of travel at higher speeds [17–19]. After the keyhole transition, L/W and L/D increase at an increasing rate with the L/D ratio being higher than the L/W ratio due to the rapid decrease in depth at speeds above the keyhole transition. At the highest speed of 2500 mm/s, the L/W ratio exceeds 5 and the L/D ratio exceeds 10. The high L/D ratio results in a microstructure with dendrites or cells that grow more vertically upward than in the lower speed welds [18].

The overall decrease in weld penetration with increasing speed is important when joining components. This effect has been studied analytically and numerically on many occasions, and a brief summary of some of the early modeling efforts are discussed elsewhere [14], while examples of more modern models are discussed in Refs. [12,17–19]. For keyhole electron beam welds in aluminum and stainless steel, the weld depth was experimentally shown to decrease inversely with travel speed to the 0.625 power for constant power welds [14,35]. Fig. 6 plots the weld depth (solid circles) for the U6Nb laser welds made in this study as a function of laser weld travel speed from 20 to 2500 mm/s on log-log coordinates, showing a similar decreasing trend. A slope of 0.625 is indicated on this figure, representative of the keyhole electron beam welds from other studies for comparison [14,35]. The U6Nb laser keyhole welds made here have a downward slope that changes from a magnitude of about 0.5 at low speeds up to about 1.0 above the keyhole transition. Near the keyhole transition, the slope matches the electron beam welds in stainless steel and aluminum with a decreasing slope of about 0.63. Given the difference in materials and process conditions, this correlation is surprisingly good, and provides additional evidence for the formation of relationships between weld penetration and welding speed over a wide range of parameters.

The coupled thermal fluids numerical weld model was used to calculate time-temperature plots during heating and cooling cycle of the welds. Fig. 8a plots these results for the slowest speed weld at 20 mm/s at the top back center of the weld where the solidification speed is the highest for the weld. Heating is very fast to the peak temperature of 4400 °C, which is the boiling point of uranium. The subsequent cooling rate is temperature dependent, being higher at higher temperatures. In this calculation, it is clear that cooling is very fast down to the liquidus temperature, T_L , of 1350 °C, where a solidification arrest begins as the melt goes through the mushy zone and latent heat of fusion is released. After solidification, cooling continues in the solid phase at a lower rate as the temperature drops below the solidus, T_S , and eventually cools to room temperature. The cooling rate is defined as the slope of this curve and is most important near the solidus temperature since this has the largest influence on the solidification microstructures that form.

The calculated cooling rates are summarized in Table 5, which gives them at three locations in each of the six welds. The three locations that were modeled for each weld pool are schematically shown in Table 5 as: a) top center, b) top edge, and c) weld center. The cooling rates at 20 mm/s varied between 5300 °C/s and 7600 °C/s, with the lower cooling rate being in the central portion

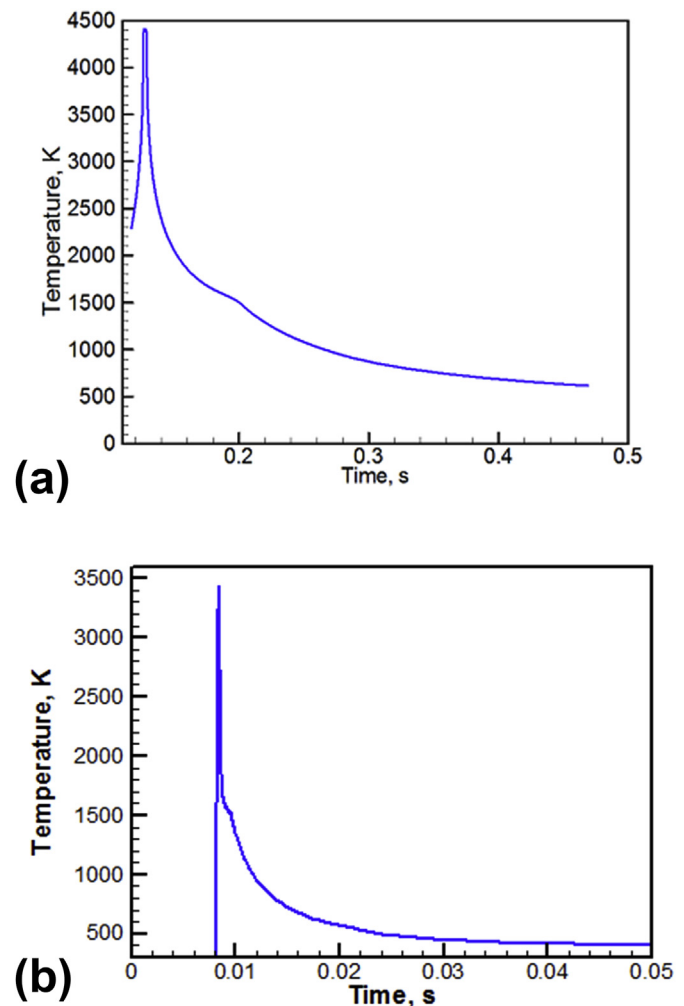
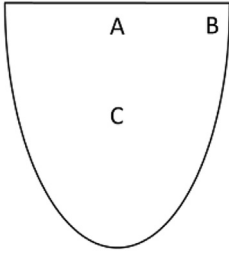


Fig. 8. Calculated time-temperature profile of a) the slowest weld at 20 mm/s, and b) the fastest weld at 2500 mm/s at the top back center of the weld pool where solidification speeds are the highest. Solidification arrests form in the mushy zone below the melting point 1623 K. Note the 10x change in time scales on the x-axis.

of the weld. At 40 mm/s the cooling rates are approximately 2x that of the 20 mm/s weld with a peak cooling rate of 15,500 °C/s. It is important to note that the cooling rates reported here were averaged over the temperature range of 1230 °C–727 °C. This temperature range has a similar slope, and thus similar cooling rate, as that of the temperature time plot through the solidification arrest region of the cooling curve. Fig. 8b shows the corresponding time temperature plot for the 2500 mm/s weld for comparison. This profile has similar peak temperatures and also has a solidification arrest, but the time scale is highly compressed due to the high speeds and high thermal gradients. Several additional high-speed U6Nb welds were numerically modeled near the keyhole transition, and also at the highest speed weld made in this study. Table 5 summarizes these data for welds made at 157 mm/s, 650 mm/s, 800 mm/s and at the highest speed of 2500 mm/s. As the speed is increased, the cooling rate at a given weld location is shown to increase at a higher rate than the increase in speed. Cooling rates on the order of 5×10^5 °C/s are calculated near the keyhole transition (700 mm/s), and on the order of 2.5×10^6 °C/s in the highest speed weld (2500 mm/s). The six cooling rate data points are plotted in Fig. 9a vs. laser scan speed, which show linear relationships on semi-log coordinates between scan speed and cooling rate, but with a change in slope at the keyhole transition. Linear fitting

Table 5

Calculated cooling rates in the temperature range 1230–727 °C, at three different locations (“a” top center, “b” top edge, and “c” near weld center) in selected welds made at different speeds.

	Weld Speed (mm/s)	Cooling Rate (°C/s) at Location		
		A	B	C
	20	7600	5320	7100
	40	15,500	10,850	15,000
	157	59,000	51,000	64,000
	650	320,000	300,000	320,000
	800	520,000	530,000	540,000
	2500	2,400,000	2,900,000	2,400,000

coefficients, shown on the plot, are given for the two modes and were used to estimate the cooling rate of the other welds that were made in this study. The results for all of the welds are plotted in Fig. 9b in log-log coordinates, showing a >300x increase in cooling rate from the lowest to the highest speed welds made in this study. This large change in cooling rate has a dramatic effect on the microstructure of the welds as will be discussed below.

3.2. The influence of weld speed and cooling rate on microstructure of U6Nb

Although welding of uranium alloys has been performed in the past, these studies have focused mainly on the macroscopic weld joint characteristics such as weld penetration, defects, and mechanical properties [4–6]. Comparatively very little work has been performed to characterize the weld FZ microstructures of uranium alloys in general, and even less for U6Nb, which is an alloy system known to form metastable phases if rapidly cooled from elevated temperatures [1–3,36]. One of the objectives in this study was to investigate the FZ microstructures of U6Nb to understand the effects of welding speed, and associated cooling rate, on microstructural evolution in U6Nb.

Fig. 10 shows a portion of an optical metallographic cross section of the 40 mm/s weld. This weld has a well-defined FZ boundary that transitions to dendrites with clearly visible secondary arms within 50 μm from the edge of the weld. The dendritic structure extends for approximately 300 μm before refining in size towards the center of the weld. This microstructure is typical of the other slow speed U6Nb welds, where the dendrites refine in size as the local solidification velocity increases due to the curvature of the weld pool [17,18]. With increasing solidification velocity, the dendrites refine and/or reorient to the point where they no longer have well-defined secondary arms and a more cellular appearing microstructure occurs. Isolated dendrites can be seen, however, in random patches in the weld FZ, as indicated by the coarse features in the full weld cross section shown in Fig. 3a. These features appear to be equiaxed dendrites and will be discussed in more detail later. Microhardness measurements made on the slow speed welds showed the FZ hardness to be 194 ± 9 DPH, the edge of the FZ to be 221 ± 24 DPH, and the cast base metal to be 150 ± 13 DPH.

SEM images of the edge of the 20 mm/s weld at higher magnifications are presented in Fig. 11, which shows some features that are not typical of welds in more conventional metals. Fig. 11a is taken at the edge of the weld with the base metal in the lower right-hand corner, at a magnification that spans the weld edge into the beginning of the dendritic microstructure. The nearly featureless base metal at this magnification clearly demarks the edge of the weld fusion zone. The transition from the base metal to the weld shows an unusual microstructure consisting of interpenetrating dark and light contrasting phases with a width of

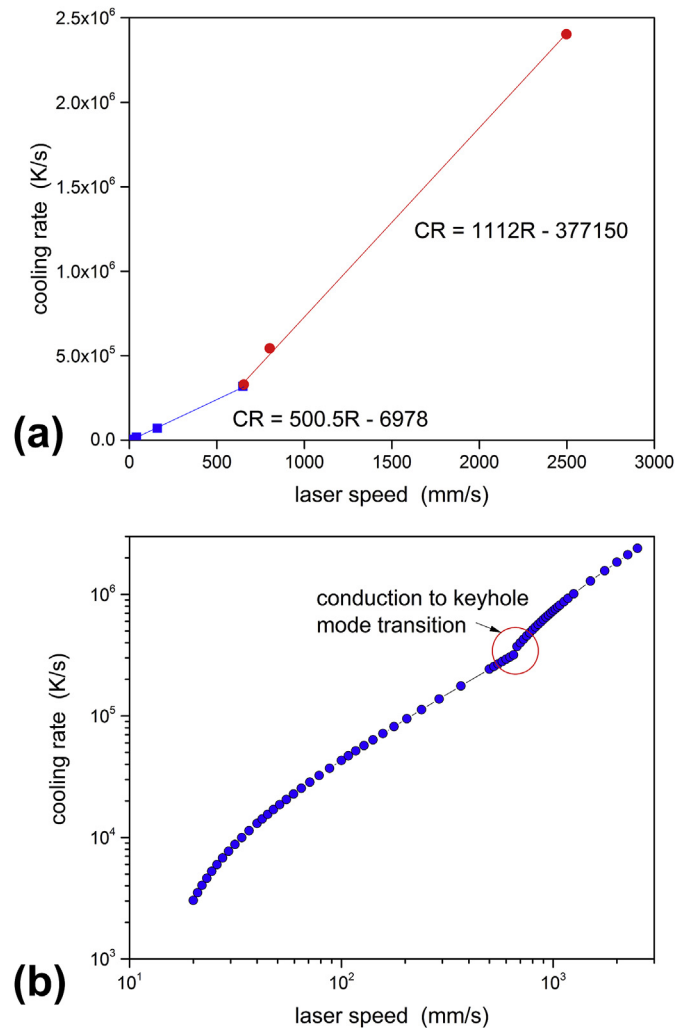


Fig. 9. a) Calculated cooling rates at the center of each of the 6 welds that were numerically modeled, with linear trend lines above and below keyhole transition, and b) interpolated cooling rates for all of the scan speeds based on the trend lines, plotted on log-log coordinates.

approximately 15 μm as shown at a higher magnification in Fig. 11b. The transition region between the base metal and the dendrites that form would normally start off as cells that epitaxially grow from the base metal [20,37]. However, in the U6Nb we do not see clearly defined classical cells [15,36] for the initial 15 μm or so before dendrites appear. Although the exact mechanism for the formation of this microstructure is not understood at this time, it

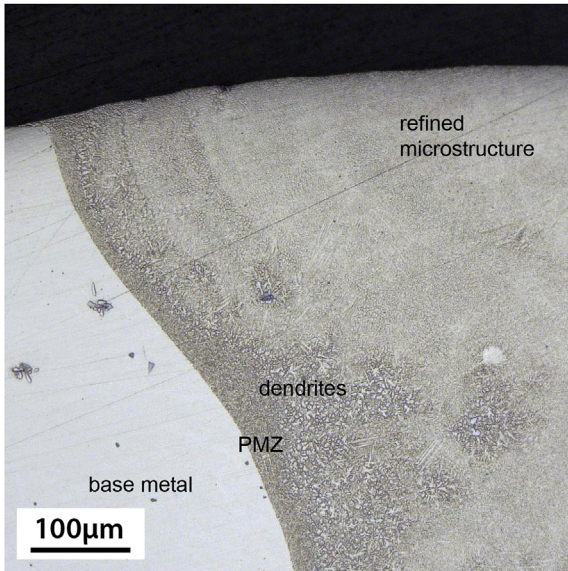


Fig. 10. Optical micrograph of the 40 mm/s weld, showing dendrites forming from the PMZ, and a more refined microstructure in the top central portion of the weld.

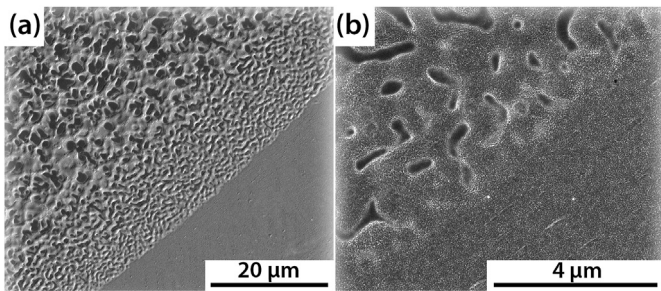


Fig. 11. SEM images taken near the edge of the 20 mm/s weld. a) The transition from base metal to dendritic structure, and b) the edge of the fusion zone boundary at higher magnifications.

may be related to a partially melted zone (PMZ), which forms in alloys with a significant difference between the liquidus and solidus temperatures. In U6Nb, this temperature difference is reasonably large at 123 °C as indicated by the in Table 3 and shown in the binary alloy phase diagram in Fig. 12 [38]. In this figure the vertical red line indicates the U6Nb composition, and the horizontal red line indicates the composition of the first solid to form during solidification at the dendrite core. This solidification temperature range can create localized melting in the low Nb regions, producing a mushy zone between the liquidus and solidus temperatures, with a maximum segregated Nb content of approximately 25 at% (~12 wt %) Nb. In addition, any localized composition gradients that are present in the base metal will accentuate this behavior and would be expected due to the as-cast condition of the starting base metal plate. Dendrites form from this zone, where the darker appearing phase was identified to be the Nb rich as determined by microprobe analysis and represents the dendrite cores.

SEM images of the 40 mm/s weld are shown in Fig. 13a at the weld edge where the microstructure is similar to the 20 mm/s weld but with a narrower PMZ region. Also present is evidence of base metal segregation in this region of the base metal where localized melting appears outside the edge of the fusion zone. A dark etching intermetallic particle is present in the base metal that is most likely a carbide phase as a result of the initial ingot casting process [1,2].

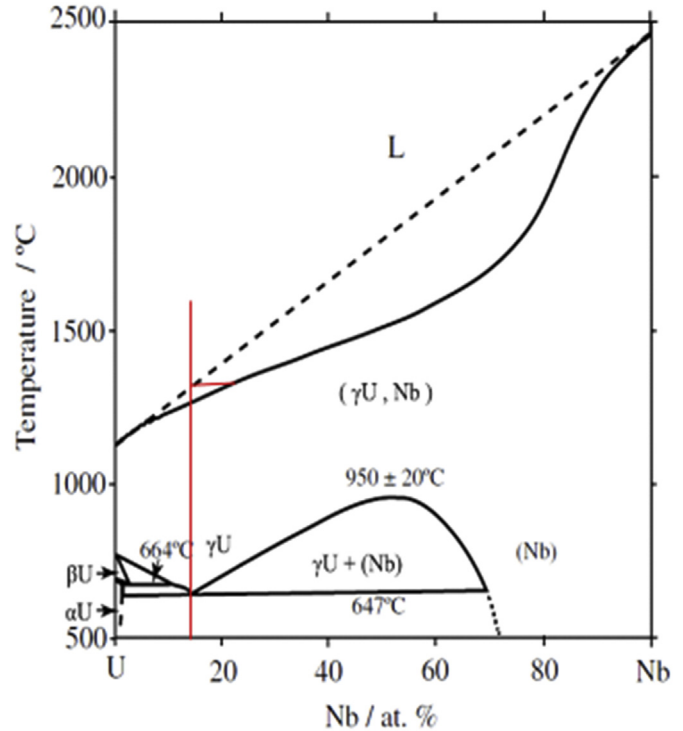


Fig. 12. U-Nb binary phase diagram with the U6wt%Nb (14.2 at% Nb) composition marked as the vertical red line, and the maximum Nb content of the first solid to form during solidification indicated by the horizontal red line. (For interpretation of the references to color in this figure legend, the reader is referred to the Web version of this article.)

Fig. 13b shows the microstructure near the center of this weld where the microstructure is refined to a size of about 1 μm cells or dendrites without prominent secondary arms.

The microstructures that form at the edge in the higher speed conduction mode welds are quite different from the lower speed conduction welds, both macroscopically and microscopically. In the high-speed welds, the PMZ reduces in size to just a few microns, while the dendritic structure largely disappears and is replaced by solidification bands forming parallel to the solidification front. This microstructure is quite different than conventional dendrites or cells that have growth directions perpendicular to the solidification front. The solidification bands appear as azimuthal lines with smaller radii towards the top center of the weld cross section as seen in Fig. 14 for a weld made at 2500 mm/s. Swirl patterns in the weld indicate that convection is occurring, and that mixing in the liquid weld pool is incomplete. Fig. 14 shows the banding phenomena, where the bands are spaced approximately 0.25 μm apart.

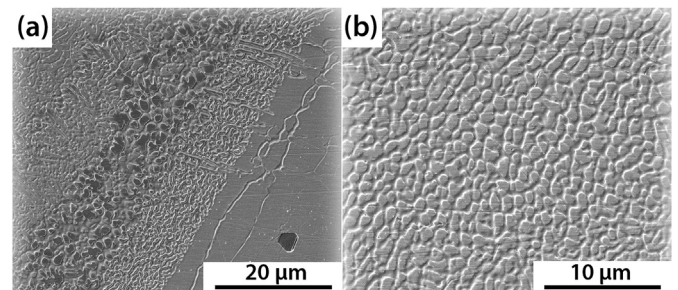


Fig. 13. SEM images taken from the 40 mm/s weld. a) The weld edge region transitioning into dendrites, and b) the refined microstructure near the central portion of the weld with no visible secondary dendrite arms.

These bands are common in all the high speed U6Nb welds and were also observed in some of the spikes at the root of keyhole welds, where the spikes presumably cool at a much higher rate than the steady state portions of the weld. Fig. 15 shows these bands more clearly in an SEM image taken at the root of the weld made at 800 mm/s. At 800 mm/s, the bands have a wider spacing than at 2500 mm/s of approximately $0.5 \mu\text{m}$, and break down into elongated cell-like structures with evidence of intercellular instability in the solidification direction in places. Microhardness measurements made on the 2500 mm/s weld showed the FZ hardness to be 154 ± 19 DPH, which is similar to the cast base metal DPH.

Images from the spiked region at the root of the 40 mm/s weld are shown in Fig. 16a. A zoomed in portion of the weld root is shown in Fig. 16b indicating the formation of very fine solidification bands in the lower left-hand side of the image. The bands have a spacing of approximately $1 \mu\text{m}$, and presumably form at much higher cooling rates than the remainder of the weld due to the transient nature of the weld spike. This band formation has the appearance of an oscillatory plane front solidification condition, possibly similar to what has been observed in a few other rapidly solidified alloy systems [39,40]. One of these studies showed solidification bands forming in the Al–Cu binary system under high speed laser scanning, where micron spaced bands formed at about 0.5 m/s scan speeds through a non-steady-state solidification mechanism [40]. Although the U6Nb binary system is different than the Al–Cu system in many ways, it is interesting to note that both alloy systems show similar banding features at similar scan speeds, and that both have large melting point differences and large density differences between their respective elements. Additional work is required to see if the bands forming in U6Nb may be related to a similar non-steady-state solidification mechanism, or if this is a peculiarity of U–Nb binary alloys.

In all of the low speed keyhole welds, and in some of the conduction welds, patches of dendrites can appear in the bulk portions of the weld microstructure. Macroscopically, these patches appear as the coarser features in the weld cross section shown in Fig. 10. The dendrites tend to occur along weld cross-sectional contours but can also occur in occasional isolated patches surrounded by cellular like features. Fig. 17a shows this behavior near the center of a weld made at 289 mm/s, where the elongated cells growing from the weld edges are surrounding a different microstructure that appears dendritic in nature. At even higher speeds of 1000 mm/s, near the keyhole to conduction mode transition shown in Fig. 17b, elongated cells from the edge of the weld are converging around a dendritic patch with well-defined secondary arms. It's not perfectly clear how these patches are forming. They may be related to weld pool perturbations that affect local G and R solidification conditions, solute segregation, and/or detached dendrite tips that are

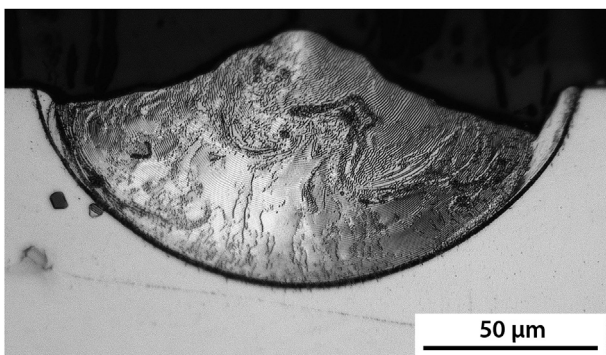


Fig. 14. Optical micrograph of the 2500 mm/s weld showing convective mixing swirls and solidification banding.

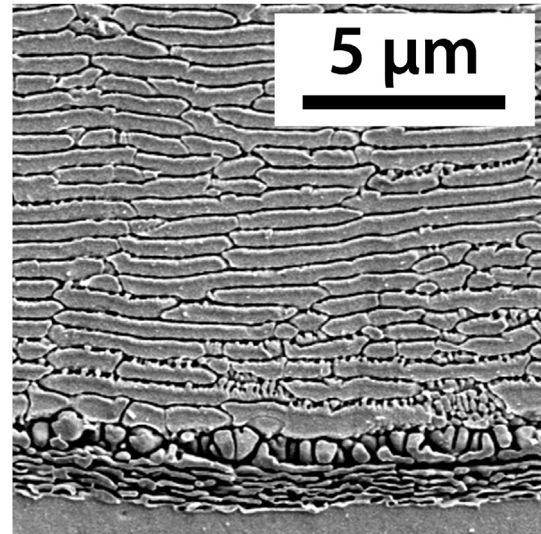


Fig. 15. SEM images of the banded microstructure forming at the root of the 800 mm/s weld.

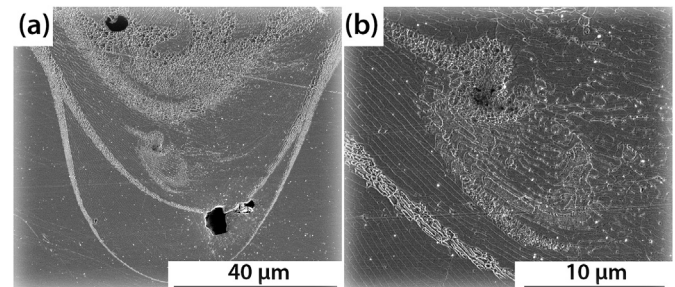


Fig. 16. a) SEM image of a transient spike in the root of the 40 mm/s weld, and b) a zoomed in region showing solidification bands and cells in the spiked region of the weld.

transported by convection to the more refined region of the weld to form equiaxed dendrites. Also seen in the upper right-hand side of Fig. 17a are fine precipitates at the boundaries of the coarser cells. These small precipitates were shown to be Nb-rich. The formation of these precipitates, along with additional characterization of the microstructural features is required to better understand how this microstructure is forming.

During weld solidification, Nb can segregate to form regions of higher than nominal concentrations. Microsegregation of this type increases at lower weld speeds where larger fusion zones are

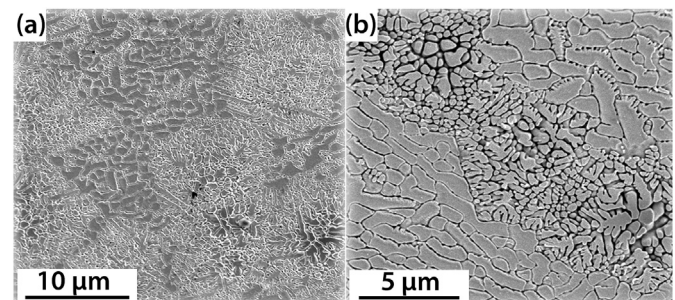


Fig. 17. SEM images of the isolated dendrite patches in a) the central portion of a weld made at 289 mm/s, and b) the top portion of a weld made at 800 mm/s.

produced and where the cooling rates are slower. To measure this effect, a low speed weld (100 mm/s) and a high-speed weld (1025 mm/s) were analyzed by electron probe micro analysis (EPMA). These results are shown in Fig. 18, where EPMA scans (blue lines) were made from the base metal and into the fusion zone. The low speed weld is shown in Fig. 18a, where the scan traverses dendrites near the fusion boundary and into the more refined cellular microstructure further into the fusion zone. The Nb concentration is shown on the plot on the right-hand side of the figure, and is made up of three distinct zones. In the base metal the Nb concentration is constant, varying only a few tenths of a percent; in the dendritic region, the Nb concentration varies considerably, with up to 2x the nominal Nb concentration; while in the cellular region the Nb concentration shows an intermediate level of variation of a few percent above and below the nominal concentration. The higher concentration of Nb would be expected at the cores of the dendrites, which are enriched in Nb as indicated in Fig. 12. Given the spot size of the EPMA beam of approximately 1 μm , the Nb variation observed in the slow speed weld with primary arm spacing larger than 1 μm is most likely due to segregation that occurs during solidification. The high-speed weld shown in Fig. 18b with a highly refined microstructure shows Nb variations constant to within a few tenths of a percent in the base metal and in the

fusion zone. However the EPMA spot size of approximately 1 μm is too large to measure segregation on the finer scale that was produced in the high-speed weld, resulting in an averaging of the composition gradients and the consequent flat measured Nb concentration profile.

The preceding sections demonstrated that the microstructures that form in the U6Nb welds vary considerably as the scan speed is increased, and also show that some of the microstructures that form are non-traditional when compared to more commonly welded materials. In terms of solidification related material properties, one factor that is important is the scale of the microstructural features, which refines with increasing scan speed and cooling rate. In U6Nb there is also a refinement of the microstructure with increasing scan speed, but because of some of the unusual microstructural features the refinement isn't as easily quantified as in more conventional alloy systems. Here we measure three microstructural parameters: the primary and secondary dendrite arm spacing where dendrites are present and clearly defined, and a "solidification band" spacing which forms in the higher speed welds. These data are plotted in Fig. 19a versus the scan speeds showing the trends on log-log coordinates to linearize the data. Each data set is fit to a relationship between microstructure scale and cooling rate as follows:

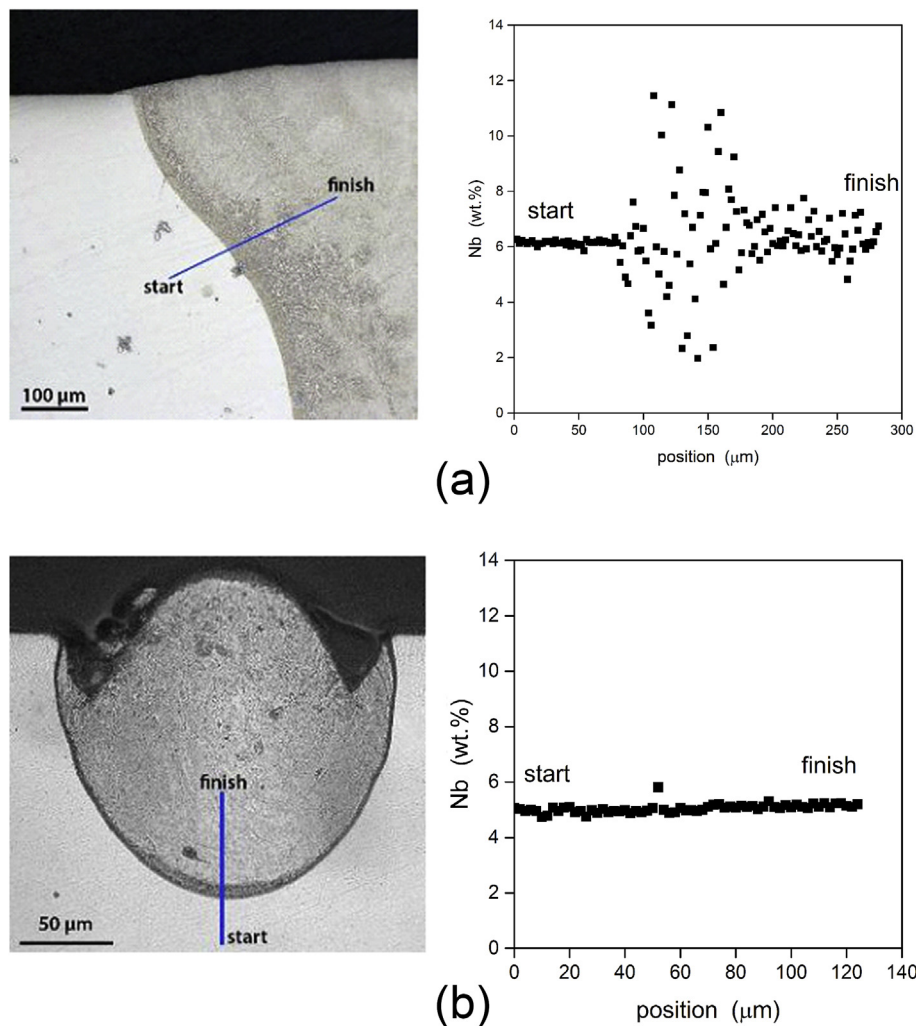


Fig. 18. Electron microprobe traverse (blue lines) with an $\sim 1 \mu\text{m}$ diameter beam showing the Nb concentration across the fusion boundary for: a) a low speed keyhole weld (100 mm/s) with a dendritic microstructure near the fusion boundary, and b) a high-speed conduction mode weld (1025 mm/s). (For interpretation of the references to color in this figure legend, the reader is referred to the Web version of this article.)

$$\lambda = c (\epsilon)^{-n} \tag{7}$$

In this equation, λ represents the dendrite arm, cell, or solidification band spacing size, ϵ , is the cooling rate, c is a constant, and n is the cooling-rate exponent that can be found from the slope of a cooling rate vs. microstructural scale plot [41]. Since the scan speed and the cooling rate of the welds are related, it is sometimes useful to develop microstructural relationships for both parameters. The cooling rate exponent of eq. (7) is known to vary from about $n = 0.28$ to $n = 0.5$ for conventional alloys such as stainless steel and aluminum alloys [20,37,41–43], where the lower end is usually associated with cells or secondary dendrite arms ($n \sim 0.33$), and the higher end is associated with primary dendrite arm spacing ($n = 0.5$) [41].

Analysis of Fig. 19a shows an overall microstructure refinement of approximately 10x from the low (20 mm/s) to the high-speed welds (2500 mm/s), with different microstructural features appearing over this range. The primary dendrite arm spacing vs. scan speed is plotted as the circles in Fig. 19a, and the best fit to this data shows that the scan speed exponent is $n = 0.535$, with an R^2 value of 0.969 as summarized in Table 6. The secondary dendrite arm spacing is shown as triangles in this plot and has a scan speed

rate exponent of $n = 0.433$ with $R^2 = 0.905$. The third set of data in Fig. 19a plots the solidification band spacing and is significantly shifted to larger spacing at a given speed than the primary or secondary dendrite arms. The band spacing has a scan speed exponent of $n = 0.284$ on this plot with $R^2 = 0.737$. The change in the scan speed exponent and the larger spacing indicate that the solidification bands are forming by a different mechanism than the dendrites or cells, which is also obvious in the microstructural features that have been presented.

Traditional relationships that explain the refinement of dendrites and cells during welding have been made using correlations between the cooling rate, rather than scan speed, to the microstructure [37]. The same type of cooling rate relationships were made here using the numerical calculations presented earlier. The results show that the cooling rate of the welds do not follow a 1:1 relationship with the laser scan speed, and that the conduction and keyhole welds follow different cooling rate trends with laser scan speed (see Fig. 9a and b for example). To take this into account, the six welds that were numerically modeled for cooling rates were used to plot the primary and secondary dendrite arm spacing, and the band spacing, versus cooling rate instead of scan speed. These data are shown in Fig. 19b, and the results for each microstructural feature are summarized in Table 6. Even though less data is presented, the trends are similar to the data plotted versus laser scan speed, with similar cooling rate coefficients whereby the cooling rate exponent $n = 0.465$ with $R^2 = 0.969$ for the primary arms, $n = 0.375$ with $R^2 = 0.915$ for the secondary arms, and $n = 0.236$ with $R^2 = 0.742$ for the solidification band spacing. Using these data, and the pre-exponential values shown in Table 6, the cooling rate of all of the welds can be estimated from the microstructure of U6Nb over the full range of scan speeds and cooling rates. It should be noted that eq. (7) is a simplified relationship for microstructure scale where G and R are combined into the cooling rate. Other relationships exist that allow G and R to be treated independently [37], and could further be used to understand the effect of scans speed on both the conventional and non-conventional microstructures that were shown to form in U6Nb.

4. Conclusions

1. A solid-state fiber laser was used to make welds on an as-cast U6Nb alloy with a fixed laser power of 400 W and travel speeds from 20 to 2500 mm/s. The laser had a 0.076 mm diameter beam and produced welds that varied in depth from 1.25 mm to 0.057 mm. The weld depths were shown to decrease inversely with increasing travel speed raised to the 0.5 power at low speeds, to the 1.0 power at high speeds, and with a value of approximately 0.63 at intermediate speeds near the keyhole to conduction mode transition.

Table 6

Summary of the microstructure refinement parameters fit by eq. (7) for the data presented in Fig. 19. c is the pre-exponential constant, n is the cooling rate exponent, and R^2 is the correlation coefficient for the best fit lines through the data.

Microstructural feature	c (μm)	n	R^2
From Laser Scan Speed (Fig. 19a)			
Primary arms	7.32	0.535	0.969
Secondary arms	2.82	0.433	0.905
Band spacing	4.62	0.284	0.737
From Calculated Cooling Rate (Fig. 19b)			
Primary arms	90.8	0.465	0.969
Secondary Arms	21.5	0.375	0.915
Band spacing	15.4	0.236	0.742

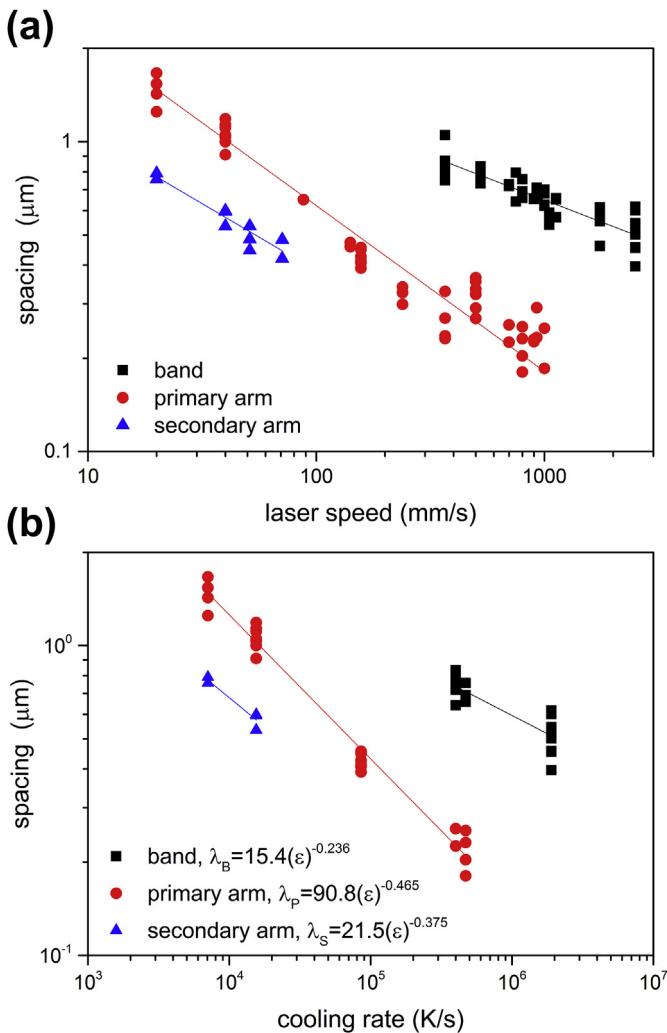


Fig. 19. Primary and secondary dendrite arm spacing and solidification band spacing measurements plotted on log-log coordinates versus: a) the laser scan speed, and b) the calculated cooling rate in the center of the six welds that were numerically modeled. Best fit parameters to the cooling rate data are indicated.

2. Keyhole welds, with aspect ratios (D/W) of approximately 1, were observed at slower speeds, but transitioned to conduction mode welds at speeds of approximately 700 mm/s and higher. The transition from keyhole to conduction mode occurred at an average energy per unit area of $E_0 = 7.5 \text{ J/mm}^2$, which is similar to electron beam welds made in stainless steel and aluminum alloys. Spiking was observed at the root of the slow speed keyhole welds with occasional root porosity, while undercutting and humping were observed in the high-speed conduction mode welds.
3. Two additional aspect ratios of the weld geometry were measured relating to the ratios of the depth, width, and length of the welds. The L/W and L/D aspect ratios behaved differently than D/W . The L/W ratio increased to values greater than 5, while L/D increased to values greater than 10 after the keyhole transition. These increases are largely due to the elongation of the weld pool shape from circular at low speeds to tear drop at high speeds on the top surface of the weld.
4. A coupled thermal fluids numerical weld model was used to calculate cooling rates in selected welds, showing a $>300\times$ increase in cooling rate for all weld pool locations as the speed was increased from 20 to 2500 mm/s. Additional results show that the travel speed is the dominant factor in controlling the cooling rate, with specific FZ weld locations being a lesser factor as detailed in Table 5.
5. Microstructures that form in the U6Nb keyhole welds at slower scan speeds show an unusual weld boundary that doesn't have the conventional appearance of epitaxial regrowth followed by the initial formation of cells. Instead, the weld edge consists of interpenetrating dark and light imaging phases before dendrites appear. It is believed that this microstructure is related to a partially melted zone as a result of the large difference between the liquidus and solidus temperatures in U6Nb, combined with the large density difference between the two metals.
6. Microstructures inside the weld PMZ boundary in the remainder of the keyhole weld fusion zone show dendrites with secondary arms forming near the weld edge, and refinement of the dendrites at the top center of the weld where secondary arms disappear and a cell like structure remains. Occasional patches of dendrites with secondary arms can also form in the FZ, surrounded by cell like features. It is speculated that the patches form as equiaxed dendrites that are related to local solidification changes in G and R , and/or a dendrite fragmentation mechanism. Regions where dendrites are present were shown to have microsegregation, with up to $2\times$ the nominal Nb concentration at the dendrite cores.
7. An unusual solidification banded microstructure appears in the conduction mode welds at speeds $>700 \text{ mm/s}$, and in the unstable spiked region of some of the keyhole welds. The banding occurs with spacing on the order of $0.5 \mu\text{m}$. In the high-speed welds, the bands break down azimuthally into elongated cell-like structures with evidence of intercellular instability in the solidification direction. In addition, at the highest speeds, macroscopic incomplete mixing was observed in the melt pool as evidenced by convection swirls. Solidification band formation in the UNb system will require additional work to understand the mechanism responsible for its formation.
8. Microstructure refinement of approximately $10\times$ was shown to occur as the scan speed increased from 20 mm/s to 2500 mm/s , and the corresponding calculated cooling rate, ϵ , increased from $7.1 \times 10^3 \text{ K/s}$ to $2.4 \times 10^6 \text{ K/s}$. These results were correlated with the primary and secondary dendrite arm spacing, and solidification band spacing, to the weld cooling rates and are described by the following relationships:

$$\lambda_P = 90.8 (\epsilon)^{-0.465} \quad (8)$$

$$\lambda_S = 21.5 (\epsilon)^{-0.375} \quad (9)$$

$$\lambda_B = 15.4 (\epsilon)^{-0.236} \quad (10)$$

In these equations, the subscripts P, S, and B, refer to primary dendrite arms, secondary dendrite arms and the solidification band spacing respectively, for spacing λ , in μm , and cooling rate, ϵ , in K/s .

Acknowledgments

This work was performed under the auspices of the U.S. Department of Energy by Lawrence Livermore National Laboratory under Contract DE-AC52-07NA27344. The authors gratefully acknowledge Paul Alexander for running the laser scanning experiments in the SLM machine, Dione Ancheta for materials handling and transfer, Dennis Wilson, Greg Smith and John Karle for sample machining, Edwin Sedillo for metallographic sample preparation and scanning electron microscopy, Nick Teslich for SEM/focused ion milling, Frederick Ryerson for electron microprobe analysis and Sabrina Fletcher for graphical art in Figs. 1 and 5.

References

- [1] R.E. Hackenberg, D.W. Brown, A.J. Clarke, L.B. Dauelsberg, R.D. Field, W.L. Hults, A.M. Kelly, M.F. Lopez, D.F. Teter, D.J. Thoma, T.J. Tucker, C.J. Vigil, H.M. Volz, U-nb Aging Final Report, Report No. LA-14327, Los Alamos National Laboratory, May, 2007.
- [2] C.M. Cady, G.T. Gray III, S.R. Chen, E.K. Cerreta, C.P. Trujillo, M.F. Lopez, R.M. Aikin, D.R. Korzekwa, A.M. Kelly, The Mechanical Response of a Uranium-niobium Alloy: a Comparison of Cast versus Wrought Processing. LA-UR-09-00920, Los Alamos National Laboratory, 2009.
- [3] A.S. Wu, D.W. Brown, B. Clausen, J.W. Elmer, The influence of impurities on the structure and mechanical properties of additively manufactured U-14 at.% Nb alloy, Scripta Materialia 130 (2017) 59–63.
- [4] T.B. Scott, J.R. Petherbridge, I. Findlay, J. Glascott, G.C. Allen, Recrystallization of uranium resulting from electron beam welding, J. Alloy. Comp. 475 (2009) 766–772.
- [5] R.D. Field, R.J. McCabe, D.J. Alexander, D.F. Teter, Deformation twinning and twinning related fracture in coarse-grained alpha-uranium, J. Nucl. Mater. 392 (2009) 105–113.
- [6] J.W. Elmer, P. Terrill, D. Brasher, D. Butler, Joining depleted uranium to high-strength aluminum using an explosively clad niobium interlayer, Weld. J. 81 (8) (2002), 167s–173-s.
- [7] K.-H. Kim, J.-H. Kim, S.-J. Oh, J.-W. Lee, H.J. Lee, C.-B. Lee, Fabrication of U-1-wt % Zr metallic fuel rodlets for irradiation test in BOR-60 fast reactor, Science and Technology of Nuclear Installations (2016) 7. Article ID 4385925.
- [8] P.W. Turner, A.B. Townsend, Welding Uranium with a Multikilowatt, Continuous Wave, Carbon-dioxide Laser Welder, Oak Ridge Y-12 Plant publication Y-2079, June, 1977.
- [9] S. Katayama, Y. Kobayashi, M. Mizutani, A. Matsunawa, Effect of vacuum on penetration and defects in laser welding, J. Laser Appl. V15 (5) (2001) 187–192.
- [10] M. Sokolov, A. Salminen, S. Katayama, Reduced pressure welding of thick section structural steel, J. Mater. Process. Technol. V219 (2015) 278–285.
- [11] J.W. Elmer, J. Vaja, H.D. Carlton, The effect of reduced pressure on laser weld porosity and weld geometry in commercially pure titanium and nickel, Weld. J. 95 (11) (2016) 419s–430s.
- [12] R. Rai, J.W. Elmer, T.A. Palmer, T. DebRoy, Heat transfer and fluid flow during keyhole mode laser welding of tantalum, Ti-6Al-4V, 304L stainless steel and vanadium, J. Phys. Appl. Phys. 40 (18) (2007) 5753–5766.
- [13] W.E. King, et al., Observation of keyhole-mode laser melting in laser powder-bed fusion additive manufacturing, J. Mater. Process. Technol. 214 (2014) 2915–2925.
- [14] J.W. Elmer, W.H. Giedt, T.W. Eagar, The transition from shallow to deep penetration during electron-beam welding, Weld. J. 69 (5) (1990) 167–s.
- [15] R. Cunningham, S.P. Nara, C. Montgomery, J. Beuth, A.D. Rollett, Synchrotron-based X-ray microtomography characterization of the effect of processing variables on porosity formation in laser powder-bed additive manufacturing of Ti-6Al-4V, J. Occup. Med. V69 (3) (2017) 479–484.
- [16] S. Kou, Welding Metallurgy, second ed., Wiley-Interscience, 2002.
- [17] H.L. Wei, J.W. Elmer, T. DebRoy, Origin of grain orientation during solidification of an aluminum alloy, Acta Mater. 115 (2016) 123–131.
- [18] H. Wei, J.W. Elmer, T. DebRoy, Three dimensional modeling of grain structure evolution during localized solidification of an aluminum alloy, Acta Math. V126 (2017) 413–425.

- [19] T.M. Rodgers, J.D. Madison, V. Tikare, M.C. Maguire, Predicting mesoscale microstructural evolution in electron beam welding, *J. Occup. Med.* 68 (2016) 1419–1426.
- [20] J.W. Elmer, S.M. Allen, T.W. Eagar, Microstructural development during solidification of stainless steel alloys, *Metall. Trans. A* 20A (10) (1989) 2117–2131.
- [21] K.A. Unocic, M.J. Mills, G.S. Daehn, Effect of gallium focused ion beam milling on preparation of aluminum thin foils, *J. Microsc.* 240 (3) (2010) 227–238.
- [22] K. Mundra, T. DebRoy, K.M. Kelkar, Numerical prediction of fluid flow and heat transfer in welding with a moving heat source, *Numer. Heat Tran. A* 29 (1996) 115–129.
- [23] S. Mishra, T. DebRoy, A heat-transfer and fluid-flow-based model to obtain a specific weld geometry using various combinations of welding variables, *J. Appl. Phys.* 98 (2008), Article Number: 044902.
- [24] R. Rai, S.M. Kelly, R.P. Martukanitz, T. DebRoy, A convective heat-transfer model for partial and full penetration keyhole mode laser welding of a structural steel, *Metall. Mater. Trans.* 39A (2008) 98–112.
- [25] R.J. Jackson, Rocky Flats Technical Datasheet (RFP-1613), The Dow Chemical Company, 1971.
- [26] B.A. Younglove, H.J.M. Hanley, The viscosity and thermal conductivity coefficients of gaseous and liquid argon, *J. Phys. Chem. Ref. Data* 15 (4) (1986) 1323.
- [27] T. Iida, R. Guthrie, *The Physical Properties of Liquid Metals*, Oxford Science Publications, 1988.
- [28] E.A. Brandes, G.B. Brook, *Smithell's Metals Reference Handbook*, seventh ed., Butterworth Heineemann, 1992.
- [29] A. Buch, *Pure Metal Properties*, ASM International and Freund Publishing House, Ltd., 1999.
- [30] *Thermophysical Properties of Materials for Nuclear Engineering*, International Atomic Energy Agency, Vienna, 2008. https://www-pub.iaea.org/MTCD/Publications/PDF/IAEA-THPH_web.pdf.
- [31] G. Beghi, *Gamma Phase Uranium-molybdenum Fuel Alloys*, European Atomic Energy Community, Joint Nuclear Research Center, Italy, 1968.
- [32] J.W. Elmer, P.W. Hochanadel, K. Lachenberg, Charles Caristan, T. Webber, *Introduction to High Energy Density Electron and Laser Beam Welding*, Vol 6A ASM Handbook-welding Fundamentals and Processes, ASM International, Metals Park, Ohio, Nov. 2011, pp. 507–513.
- [33] J.O. Milewski, *Additive Manufacturing of Metals*, from Fundamental Technology to Rocket Nozzles, Medical Implants, and Custom Jewelry, Springer Series in Materials Science, 2017 vol. 258.
- [34] T. DebRoy, H.L. Wei, J.S. Zuback, T. Mukherjee, J.W. Elmer, J.O. Milewski, A.M. Beese, A. Wilson-Heid, A. De, W. Zhang, Additive manufacturing of metallic components-process structure and properties, *Prog. Mater. Sci.* 92 (2018) 112–224.
- [35] W.H. Giedt, L.N. Talerico, Prediction of electron beam depth of penetration, *Weld. J.* 67 (12) (1988) 299s–305s.
- [36] K.H. Eckelmeyer, A.D. Romig Jr., L.J. Weirick, The effect of quench rate on the microstructure, mechanical properties, and corrosion behavior of U-6 Wt Pct Nb, *Metall. Mater. Trans.* 15A (1984) 1319–1330.
- [37] W. Kurz, D.J. Fisher, *Fundamentals of Solidification*, Trans Tech Publications, 1986.
- [38] J. Koike, M.E. Kassner, R.E. Tate, R.S. Rosen, in: M.E. Kassner, D.E. Peterson (Eds.), *Phase Diagrams of Binary Actinide Alloys*, ASM International, Materials Park, OH, 1995.
- [39] M. Carrard, M. Gremaud, M. Zimmermann, W. Kurz, About the banded structure in rapidly solidified dendritic and eutectic alloys, *Acta Metall. Mater.* 40 (5) (1992) 983–996.
- [40] M. Zimmermann, M. Carrard, M. Gremaud, W. Kurz, Characterization of the banded structure in rapidly solidified Al-Cu alloys, *Mater. Sci. Eng.* 134 (1991) 1278–1282.
- [41] M.C. Flemings, *Solidification Processing*, McGraw Hill Series in Materials Science and Engineering, 1974.
- [42] S. Katayama, A. Matsunawa, Solidification microstructures of laser welded stainless steels, *Proc. ICALEO 84* (1985) 60–67. Laser Institute of America, Toledo, OH.
- [43] K.P. Young, D.H. Kirkwood, The dendrite arm spacing of aluminum-copper alloys solidified under steady state conditions, *Met. Trans.* 6A (1975) 197–205.